12772 *Biochemistry* **2001,** *40,* 12772−12781

Structure of β-Ketoacyl-[acyl carrier protein] Reductase from *Escherichia coli*: Negative Cooperativity and Its Structural Basis[†,‡]

Allen C. Price,[§] Yong-Mei Zhang,[∥] Charles O. Rock,[∥,#] and Stephen W. White*,[§,#]

Department of Structural Biology and Division of Protein Science, Department of Infectious Diseases,
St. Jude Children's Research Hospital, Memphis, Tennessee 38105, and Department of Molecular Sciences,
University of Tennessee Health Science Center, Memphis, Tennessee 38163

Received April 11, 2001; Revised Manuscript Received July 13, 2001

ABSTRACT: The structure of β-ketoacyl-[acyl carrier protein] reductase (FabG) from *Escherichia coli* was determined via the multiwavelength anomalous diffraction technique using a selenomethionine-labeled crystal containing 88 selenium sites in the asymmetric unit. The comparison of the *E. coli* FabG structure with the homologous *Brassica napus* FabG·NADP$^+$ binary complex reveals that cofactor binding causes a substantial conformational change in the protein. This conformational change puts all three active-site residues (Ser 138, Tyr 151, and Lys 155) into their active configurations and provides a structural mechanism for allosteric communication between the active sites in the homotetramer. FabG exhibits negative cooperative binding of NADPH, and this effect is enhanced by the presence of acyl carrier protein (ACP). NADPH binding also increases the affinity and decreases the maximum binding of ACP to FabG. Thus, unlike other members of the short-chain dehydrogenase/reductase superfamily, FabG undergoes a substantial conformational change upon cofactor binding that organizes the active-site triad and alters the affinity of the other substrate-binding sites in the tetrameric enzyme.

Interest in bacterial fatty acid biosynthesis is increasing due both to a growing appreciation of the complexity of the pathway and to the opportunities that the participating enzymes afford as drug targets. The architecture of fatty acid synthase (FAS)[1] takes two forms in nature. The associated system, FAS I, consists of a single large polypeptide that contains multiple active sites, and which performs all of the elongation steps in the pathway (*1*). This system is primarily found in metazoans. The dissociated system, FAS II, is composed of separate proteins, and each protein carries out a different catalytic step in the pathway (*2*). This latter system is found in bacteria and plants. Because of these fundamental differences in architecture, there are inhibitors that selectively target enzymes in the bacterial FAS II system and thus act as antibacterials (*3*).

In the FAS II elongation cycle, the growing acyl chain is carried by ACP to a series of four enzymes (*2*). First, one of the β-ketoacyl-ACP synthases (FabB or FabF) elongates the acyl-ACP C_n acyl chain to a C_{n+2} β-ketoacyl form. Next, the β-keto group is reduced by the NADPH-dependent β-ketoacyl-ACP reductase (FabG, the subject of this study), and the resulting β-hydroxy intermediate is then dehydrated by the β-hydroxy acyl-ACP dehydratase (FabA or FabZ) to an enoyl-ACP. Finally, the reduction of the enoyl chain by a nucleotide cofactor dependent enoyl-ACP reductase (FabI, FabK, or FabL) produces an acyl-ACP with an elongated C_{n+2} acyl chain which is ready to reenter the cycle. Elongation ends when the acyl chain either is used for phospholipid synthesis or grows to the maximum length dictated by the length of the active-site tunnel in the synthases, FabF and FabB.

The FabG enzyme requires NADPH for its activity (*4*, *5*), has a monomeric molecular weight of about 25.5K, and exists as a tetramer in solution (*6*). The sequence reveals that the protein belongs to the short-chain dehydrogenase/reductase (SDR) family of enzymes, whose members catalyze a broad range of reduction and dehydrogenase reactions using a nucleotide cofactor (*7*). FabG is highly conserved across species and is the only known isozyme to catalyze reduction of the β-keto group. Therefore, it is an essential enzyme in bacteria (*8*) and an ideal target for the development of new antibiotics. FabG is not targeted by any known inhibitors.

In this study, we report a structure determination and biochemical analysis of FabG from *Escherichia coli*. The structure of the FabG·NADP$^+$ binary complex from *Brassica napus* has previously been determined (*9*), and a comparison with our structure of *E. coli* FabG without cofactor reveals that a substantial conformational change occurs in the enzyme upon cofactor binding. The conformational change suggests that there is allosteric regulation within the FabG

[†] This work was supported by National Institutes of Health Grant GM 45737 (C.O.R.), Cancer Center (CORE) Support Grant CA 21765, and the American Lebanese Syrian Associated Charities (ALSAC). A.C.P. is the recipient of the Richard Gephardt Postdoctoral Fellowship.

[‡] The X-ray coordinates have been deposited in the Protein Data Bank with file name 1I01.

* To whom correspondence should be addressed. Phone: (901) 495-3040. Fax: (901) 495-3032. E-mail: stephen.white@stjude.org.

[§] Department of Structural Biology.

[∥] Department of Infectious Diseases.

[#] Department of Molecular Sciences.

[1] Abbreviations: FAS, fatty acid synthase; FabG, β-ketoacyl-[acyl carrier protein] reductase; ACP, acyl carrier protein; NADP(H), nicotinamide adenine dinucleotide phosphate (reduced form); SDR, short-chain dehydrogenase/reductase; MAD, multiwavelength anomalous diffraction; NCS, noncrystallographic symmetry; ASU, asymmetric unit.

10.1021/bi010737g CCC: $20.00

Table 1: Statistics of X-ray Data Collection

	peak	remote
wavelength (Å)	0.979	0.954
resolution range (Å)	29.2−2.6 (2.74−2.60)[a]	29.2−2.6 (2.74−2.60)
reflections	175 170 (18 175)	179 428 (18 850)
unique reflections	53 360 (6937)	53 656 (7046)
completeness (%)	91.0 (81.4)	91.5 (82.7)
multiplicity	3.3 (2.6)	3.3 (2.7)
R_{merge}[b]	0.035 (0.066)	0.037 (0.078)
I/σ	11.2 (7.6)	10.2 (7.4)

[a] Values in parentheses indicate high-resolution shell. [b] $R_{\mathrm{merge}} = \sum\sum|I_i - I_m|/\sum\sum I_i$ where I_i is the intensity of the measured reflection and I_m is the mean intensity of all symmetry-related reflections.

homotetramer, which is supported by the biochemical analyses of the binding of substrate to the enzyme. A model is developed to illustrate how FabG binds cofactor and substrate that is consistent with both our structural results and our biochemical analyses.

EXPERIMENTAL PROCEDURES

Crystallization. The cloning and overexpression of the *fabG* gene, and the purification of the FabG protein, have been described elsewhere (*10*). The purified protein was dialyzed against 20 mM Tris-HCl, pH 7.9, 1 mM DTT, and 100 mM EDTA. Hanging drop vapor diffusion experiments showed that the optimal well solution for the crystallization of the unlabeled enzyme was 20% PEG-10000, 100 mM Hepes, pH 8.5. Within 2 weeks, crystals measuring 0.5 mm × 0.4 mm × 0.2 mm grew as either diamond or hexagonally shaped plates, with the (001) surface at the largest face. Attempts to crystallize complexes of protein and cofactor have so far been unsuccessful. The selenomethionine-labeled enzyme was purified and crystallized under the same conditions as the native protein.

Data Collection. All of the MAD data used in the structure determination were collected using beamline X25C at the National Synchrotron Light Source during the experimental phase of the RAPIDATA 2000 course. Beamline X25C was equipped with the Brandeis B4 detector. All crystals used for data collection were flash frozen in 50% paratone-N and 50% mineral oil, and maintained at 100 K during data acquisition. The rotation method was used to acquire 360° of data in 1° oscillations at each of two wavelengths: the peak and a high energy remote. Indexing and integration were performed using MOSFLM (*11*), and scaling of the data was performed with SCALA (*12*). The space group was determined to be $P2_1$, with unit cell parameters $a = 61.7$ Å, $b = 120.1$ Å, $c = 131.1$ Å, and $\beta = 90.5°$. The asymmetric unit (ASU) contained eight monomers. The data collection and processing statistics are found in Table 1.

Experimental Phasing. The measured structure factors were phased using the MAD technique. To determine the selenium positions, our data were first prepared for Shake and Bake v2.1 (SnB) (*13*) using the program DREAR (*14*). Eight SnB trials were performed, each with a different random number seed. Each trial produced a different list of 130 candidate peaks. The top 24, 32, 48, and 64 peaks from each trial were refined against both wavelengths of data in separate refinements using MLPHARE (*15*). None of these refinements improved the statistics. Difference maps, produced using CNS v1.0 (*16*) and examined using O (*17*), identified no new sites. Using O, the eight independent sets of peaks from the different trials were visually compared. It was discovered that there was a subset of peaks in common among the eight sets, after taking into account ambiguities of handedness and origin. To identify all the common peaks from the eight trials, one set was picked as reference, and, once the correct origin and handedness of each set had been determined, each was transformed and superimposed onto the reference set. Peaks were chosen which appeared in at least four of the eight superimposed trials. These totaled 31 sites, and these were refined against both data sets using MLPHARE. Statistics improved, and difference maps were calculated and used to identify new sites. Although the difference maps were quite noisy, the noncrystallographic symmetry (NCS) enabled us to pick new peaks from the noise. This was facilitated by noting a “constellation” of four peaks that repeated at different locations in the ASU (see Figure 1). It eventually proved that each constellation corresponded to a different monomer in its NCS site within the ASU. Crucially, peaks found in this way could also be extended to all eight NCS sites. After three iterations, this process resulted in a total of 56 sites. MLPHARE did not produce an interpretable map at this point, and no new selenium positions could be determined from further difference maps. However, refinement of the 56 sites using the program, SHARP v1.3.8β (*18*), resulted in the calculation of an interpretable experimental map using solvent flipping. The experimental map was of excellent quality as can be seen in Figure 1.

Model Building and Refinement. The experimental map clearly showed a β-sheet core in each monomer, and approximately 85% of the ASU could be built into the experimental map using the program, O. All refinement was done by simulated annealing using the program, CNS. The initial model was refined starting at 5000 K, but this starting temperature was reduced to 2500 K in later rounds. NCS restraints were used due to the large number of atoms in the ASU and the limited resolution. The residues to exclude from NCS restraints were determined by superimposing the initial models for all eight monomers in the ASU and identifying the regions of the sequence with significantly different conformations. In each round, the program O was used to examine $2mF_o - DF_c$ and $mF_o - DF_c$ maps and to rebuild the model. Due to the large number of residues in the ASU (∼2000), “site-directed” rebuilding was performed by using Ramachandran plots and other stereochemical indicators (PROCHECK (*19*)), along with extensive calculation of real space R-factors (CNS), to identify problem residues. After the first round of refinement, crystallographic R-factors were 27.3% for the working set (R_{work}) and 30.3% for the test set (R_{test}). In the second round of refinement, another 8% of the ASU was built and refined, resulting in an $R_{\mathrm{work}} = 24.5\%$ and an $R_{\mathrm{test}} = 27.3\%$. At this point, CNS was used to add water molecules that were clearly visible at 2.6 Å. Only the strongest peaks with the clearest hydrogen-bonding geometry were added, and NCS restraints were used in the positional and temperature factor refinement of equivalent waters in the eight monomers. A third and final round of positional refinement and temperature factor refinement completed the model. The final statistics of the model are shown in Table 2.

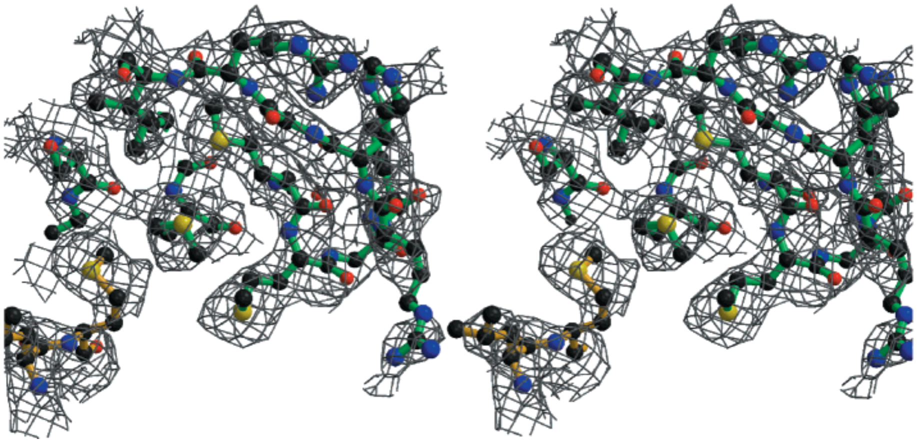

FIGURE 1: Experimental electron density map of FabG from *E. coli*. The hydrophobic clustering of selenomethionines 122, 125, 126, and 96′ is shown. The selenium atoms are colored yellow. These four selenium atoms create the constellation that was pivotal in determining the anomalous scatterers' positions (see text). The electron density is contoured at the 1σ level. The figure was created using the program BOBSCRIPT (*37*) and rendered with RASTER3D (*38*).

Table 2: Structure Refinement Statistics

resolution range of data included	29.0−2.6 Å
no. of reflections in working set (R_{work})	53156
no. of reflections in test set (R_{test})	2826
no. of protein atoms in asymmetric unit	13253
no. of water molecules in asymmetric unit	349
R_{work}	22.8%
R_{test}	25.0%
rms deviations from ideal stereochemistry	
bond lengths	0.007 Å
bond angles	1.2°
dihedrals	22.4°
impropers	0.7°
mean *B*-factor	32.2 Å^2
Ramachandran plot	
residues in most favored region	94.6%
residues in additionally allowed region	5.4%

Fluorescence Titration of FabG-NADPH Binding. Equilibrium binding of NADPH to FabG was measured by fluorescence titration using a SLM-Aminco 8100 spectrofluorimeter (Urbana, IL) at 20 °C. Increased fluorescence of NADPH upon binding to FabG was measured by exciting at 340 nm (8 nm band-pass) and monitoring the emission at 455 nm (8 nm band-pass). Aliquots of 2 μL of NADPH were added to 2 mL of 0.5 μM FabG in 0.1 M sodium phosphate buffer, pH 7.5. The solution was mixed after the addition of each aliquot, and the fluorescence intensity was recorded as the average of three readings. Effect of ACP on NADPH binding to FabG was studied by titration of NADPH into 2 mL of 0.5 μM FabG in the presence of 20 μM ACP in 0.1 M sodium phosphate buffer, pH 7.5.

Surface Plasmon Resonance Measurement of FabG-ACP Binding. Binding studies of FabG-ACP interaction were performed using a Biacore 3000 Surface Plasmon Resonance (SPR) instrument. ACP was covalently attached to a carboxymethyl-dextran coated gold surface (CM-5 Chip, Biacore). The carboxymethyl groups on the chip were activated with *N*-ethyl-*N*′-(3-dimethylaminopropyl) carbodimide and *N*-hydroxysuccinimide. The ACP was attached at pH 4.5 to this activated surface by reaction of the carboxyl groups of the dextran with primary amines on the ACP to form an amide linkage. Any remaining reactive sites on the surface were blocked by reaction with ethanolamine. A reference cell was prepared similarly except that no ACP was added. FabG stock was dialyzed against 10 mM HEPES, 150 mM NaCl, pH 7.4 (HBS-N buffer, Biacore), and diluted to desired concentrations in an HBS-N buffer containing 100 μM NADPH. Binding was measured by flowing the FabG solution at a flow rate of 20 μL/min through the reference and ACP-containing flow cells in sequence. A blank injection was also performed with an HBS-N buffer containing the same concentration of NADPH but no FabG. Following the injection, release of the bound FabG was measured by flowing only HBS-N buffer through the flow cells. Regeneration of the chip surface to remove bound FabG consisted of allowing the protein to dissociate in HBS-N buffer between injections. The data reported are the differences between the SPR signals from the ACP containing flow cell and from the reference cell. Any contribution of buffer and NADPH to the signal was removed by subtraction of the blank injection from the reference-subtracted signal. Similar experiments were performed to study the concentration dependence of the effect of NADPH on FabG-ACP binding. Instead of varying the FabG concentration, different concentrations of NADPH were added to 4.2 μM FabG. Blanks were run using buffer containing the same concentrations of NADPH.

Effect of NADPH on FabG-ACP Interactions measured by AlphaScreen. AlphaScreen technology is an experimental approach to study biochemical interactions (*20*, *21*). Upon laser excitation, a chemical signal (singlet oxygen) is generated on the donor beads (streptavidin coated). When a specific interaction brings the acceptor beads (antibody coated) to the proximity of the donor beads, energy transfer takes place, resulting in an amplified fluorescence signal at a wavelength that is lower than that of the excitation. We applied this assay system to study the protein:protein interaction between FabG and ACP. Binding between the biotinylated ACP and His-tagged FabG brings streptavidin donor beads and anti-$(\mathrm{His})_6$ antibody acceptor beads together, emitting AlphaScreen signals. To study the effect of NADPH on FabG-ACP binding, 1 μM His-tagged FabG and 1 μM biotinylated ACP were incubated at room temperature in a 384-well ProxiPlate (Packard, Canada) in the presence of different concentrations of NADPH, ranging from 0.1 to 30 μM. After a 30-min incubation, streptavidin donor beads and anti-$(\mathrm{His})_6$ antibody acceptor beads [50 μg/mL final con-

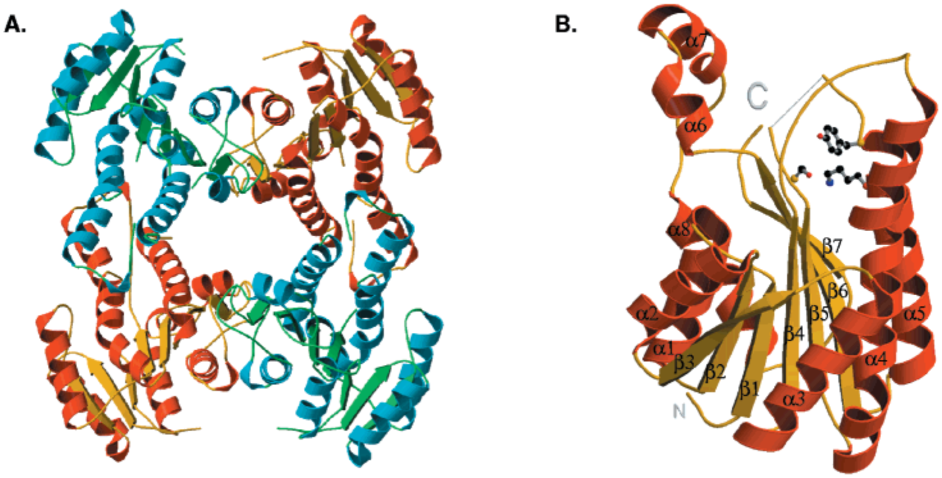

FIGURE 2: Structure of *E. coli* FabG. (A) The FabG tetramer. Monomers are shown with alternating color schemes for clarity. All β sheets are shown in yellow or green, and α helices in red or blue. (B) A ribbon diagram of the monomer showing the secondary structural elements with their conventional numbering. The amino and carboxy termini are labeled N and C, respectively. The disordered loop of residues 140−147 is indicated by a gray line. The active-site triad (Ser 138, Tyr 151, and Arg 155) is also shown. The figure was made with MOLSCRIPT (*39*) and rendered with RASTER3D (*38*).

centration for each bead, (His)$_6$Tag detection system, Packard, Canada] were added to the above solutions. The reaction mixes were then incubated for 1 h before being read by a Fusion Universal Microplate Analyzer (Packard, Canada), with excitation at 680 nm and emission at 600 nm.

RESULTS

Quality of the Structure. The quality of the final FabG structure was judged both by its stereochemical correctness and by its agreement with the data. A stereochemical analysis was performed using PROCHECK (*19*) and X-PLOR (*22*). The stereochemical statistics were better than average for a structure at this resolution (Table 2), and all residues were in the strictly and additionally allowed regions of the Ramachandran plot. The final R-factors ($R_{\text{test}} = 25.0\%$, $R_{\text{work}} = 22.8\%$) revealed how closely our final structure agreed with the data. Both were reasonable values for a structure at medium resolution, and the relatively small difference between R_{test} and R_{work} implies that there was no significant overfitting of the data. The completeness of the monomer varied between 85 and 98% among the NCS related monomers. The only region missing in all eight monomers was the loop connecting residue 140 to residue 147, which was presumed to be disordered.

Description of Structure. The structure we report of *E. coli* FabG is shown in Figure 2, and it is similar to the overall structure of the *B. napus* FabG·NADP$^+$ complex (*9*) except for a few substantial conformational differences that are discussed later. The protein contains a typical Rossmann fold structure, with a twisted, parallel β-sheet composed of seven β-strands flanked on both sides by a total of eight α helices. The core of the structure is built of two, right-handed $\beta\alpha\beta\alpha\beta$ motifs. The first is composed of strands, $\beta1$, $\beta2$, and $\beta3$, along with helices $\alpha1$ and $\alpha2$, and the second is made up of strands $\beta4$, $\beta5$, and $\beta6$, along with helices $\alpha4$ and $\alpha5$. These two motifs are connected by helix $\alpha3$. Somewhat separated from the core of the structure is a distinctive α-turn-α motif created by helices $\alpha6$ and $\alpha7$. The protein fold is completed by helix $\alpha8$, which lies adjacent to strands $\beta6$ and $\beta7$.

FabG forms a tetramer with two types of dimerization interface. One interface is located between helices $\alpha4$, $\alpha5$ and $\alpha4'$, $\alpha5'$ (primes indicate features in the neighboring monomer within the tetramer), which together form a four helix bundle. In this interface, $\alpha4$ interacts primarily with $\alpha4'$, while $\alpha5$ interacts mainly with $\alpha5'$. The $\alpha4-\alpha4'$ interaction is almost exclusively hydrophobic in nature, and comprises a number of hydrophobic clusters involving methionine residues (see Figure 1 for an example). The $\alpha5-\alpha5'$ interaction is steric. The two helices $\alpha5$ and $\alpha5'$ present a run of alanine residues that sterically complement each other. The second dimerization interface is formed between the $\beta7$ strands from each monomer, with some interactions involving the $\alpha6/\alpha7$ subdomain. This interface appears to play an important role in the NADP(H)-induced conformational change to be discussed below and is shown in Figure 3. The two β-strands run antiparallel, and the gap between them is bridged by specific side chain−side chain interactions that provide most of the interactions between the two monomers at this interface (Figure 3B). However, Tyr 129 also has an important role, as it reaches into a pocket in the opposing $\alpha6'/\alpha7'$ domain and participates in an hydrogen-bonding network (Figure 3C).

Active Site. The active-site residues (Ser 138, Tyr 151, and Lys 155) are grouped together near the loop connecting $\beta5$ and $\alpha5$ (Figure 2B). Both Tyr 151 and Lys 155 are located on helix $\alpha5$, while Ser 128 is in the loop region at the carboxy terminal end of $\beta5$. It is an unusual and consistent feature of the active site that the orientation of Tyr 151 directs its hydroxyl group away from both Ser 138 and Lys 155. Furthermore, the loop connecting the carboxy terminus of strand $\beta4$ to the amino terminus of helix $\alpha4$ lies directly over Tyr 151. In two out of the eight monomers in the asymmetric unit, this loop is stabilized by a crystal contact, and the electron density clearly shows both the conformation of the loop and the tyrosine side chain. In four of the remaining monomers, there are no crystal contacts to stabilize this loop, but although the density is weaker, it clearly shows the same orientation of Tyr 151 and the same positioning of the loop.

Conformational Changes Induced by Cofactor Binding. Recently, the structure of a plant FabG was determined (*9*), and its structure is very similar to the *E. coli* enzyme reported

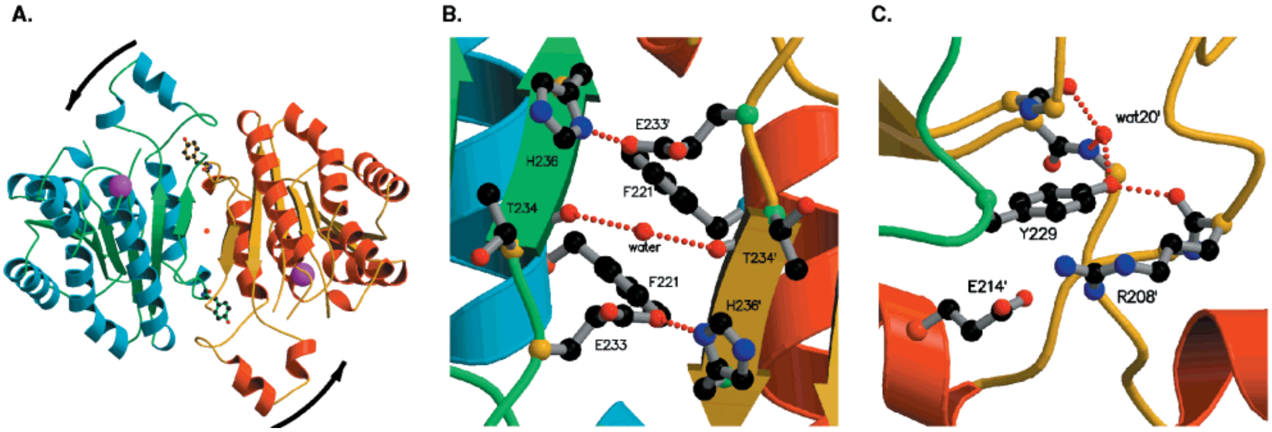

FIGURE 3: Intermolecular interactions in *E. coli* FabG. Monomers are shown with alternating color schemes for clarity. All β sheets are shown in yellow or green, and α helices in red or blue. (A) A view of two interacting monomers. The other two monomers in the foreground have been removed for clarity. The purple spheres indicate the locations of the active sites. The curved arrows indicate the direction of motion of the $\alpha6/\alpha7$ subdomain upon cofactor binding. Tyr 129 and Tyr 129′ are shown, as is the water molecule (red) on the 2-fold axis. (B) Close up view of the interactions near the 2-fold axis. (C) A close up of the insertion of Tyr 129 into the pocket on the opposing monomer (see panel A). Figure produced using MOLSCRIPT (*39*), and rendered with RASTER3D (*38*).

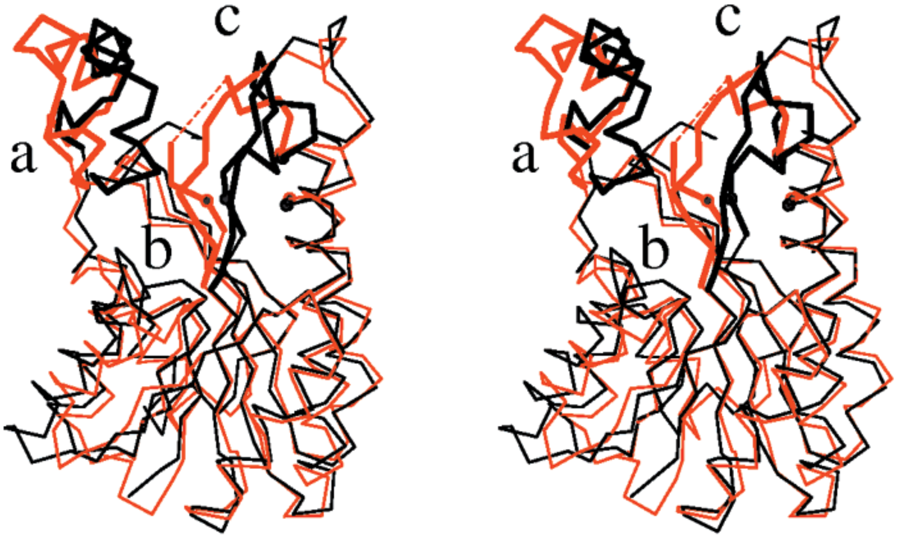

FIGURE 4: Gross conformational differences between NADP$^+$ bound and unbound forms of FabG. A stereoview of the alpha carbon traces of both *E. coli* FabG (orange) and *B. napus* FabG·NADP$^+$ (black) are shown superimposed. Areas which undergo significant conformational change are indicated by thick lines and labeled: the $\alpha6/\alpha7$ subdomain (*a*), the $\beta4-\alpha4$ loop (*b*), and the $\beta5-\alpha5$ loop (*c*). The disordered $\beta5$-$\alpha5$ loop in *E. coli* FabG (residies 140−147) is indicated by a dashed red line. The positions of the active-site residues are shown for both FabG (red circles) and FabG·NADP$^+$ (black circles). The figure was made with MOLSCRIPT (*39*).

here. The *B. napus* FabG structure is a binary complex containing bound NADP$^+$, whereas this cofactor is absent from our structure. The strong homology between the structures and sequences of *E. coli* FabG and *B. napus* FabG (49% identical) supports the conclusion that the two enzymes bind the cofactor in an identical manner. This allows us to compare the two structures to examine the conformational changes induced by cofactor binding in FabG enzymes.

A superposition of the two structures (Figure 4) reveals that the binding of NADP$^+$ is associated with significant conformational changes that can be divided into three distinct regions. The first, labeled *a* in Figure 4, is the $\alpha6/\alpha7$ subdomain that swings 9 Å as a single unit from its position in FabG to a position adjacent to the active-site cleft in the complex (see also Figure 3A). The second region, labeled *b* in Figure 4, is the loosely packed loop connecting $\beta4$ and $\alpha4$ in FabG that becomes tightly associated with $\alpha4$ in the FabG·NADP$^+$ complex. Finally, the loop between $\beta5$ and $\alpha5$, labeled *c* in Figure 4, is disordered in the FabG structure, while it forms a short helical segment that packs against helix $\alpha5$ in the FabG·NADP$^+$ structure. One effect of these concerted movements is that the distance between $\alpha6$ and the C-terminus of $\beta4$ (~8 Å) is unchanged as the two regions move together. In FabG, the $\beta4-\alpha4$ loop makes a weak contact with the $\alpha6/\alpha7$ subdomain through the hydrophobic packing of Ile 89 with Met 188. Also, the $\beta4-\alpha4$ loop makes a hydrogen bond from the backbone amide of Arg 91 to the OH group of the active-site Tyr 151. This latter residue is inserted between the $\beta4-\alpha4$ loop and the $\alpha4$ helix, preventing the two from interacting. In FabG·NADP$^+$, these weak interactions are broken, and the $\beta4-\alpha4$ loop makes a number of new interactions with helix $\alpha4$. Among these interactions are the hydrophobic packing of *bn*Ile 105 and *bn*Val 122 (residues with the *bn* prefix refer to the *B. napus* FabG sequence), a salt bridge between *bn*Arg 107 and *bn*Glu 121, and the hydrogen bonding of the backbone amide of *bn*Ile 105 to the OD1 of *bn*Asn 126. All of the residues involved in these interactions are conserved between the *E. coli* and

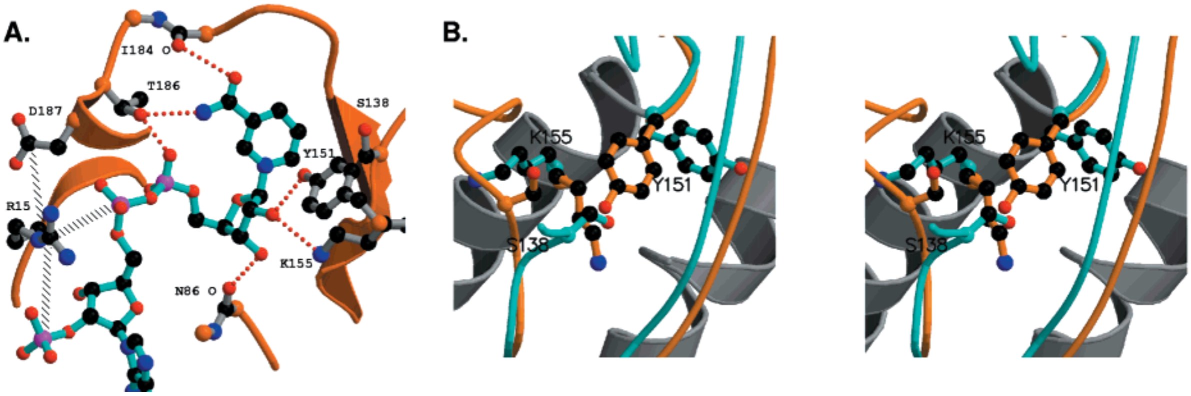

FIGURE 5: Model of the *E. coli* FabG·NADP(H) complex. (A) Interactions between NADP(H) and *E. coli* FabG. Only shown are interactions which are not possible in the free form of the enzyme. Hydrogen bonds are indicated by dotted red lines. Salt bridges are indicated by thick, hatched, black lines. The active-site triad (Ser 138, Tyr 151, Lys 155) is on the right. (B**)** Conformational changes in the active site of *E. coli* FabG induced by cofactor binding. Stereoviews of the active site of *E. coli* FabG (blue) and *E. coli* FabG·NADP(H) (modeled, orange) are shown superposed. The conformational changes in the residues are driven by cofactor binding. Figure made with MOLSCRIPT (*39*) and rendered with RASTER3D (*38*).

B. napus enzymes, except for the conservative substitutions of a valine for an isoleucine and a glutamate for an aspartate. It should be emphasized that these differences between FabG and FabG·NADP$^+$ are not crystal artifacts because they are present in comparisons with all eight monomers in the asymmetric unit of the *E. coli* FabG crystal structure.

Modeling of Cofactor Binding to E. coli FabG. To gain further insight, we modeled the binding of NADP(H) to *E. coli* FabG using the *B. napus* FabG·NADP$^+$ coordinates (*9*). Figure 5A shows a close up of the modeled *E. coli* FabG·NADP(H) interaction. All of the residues shown are strictly conserved in 11 of 11 sequences examined, with the exception of Thr 186, which is conservatively replaced by serine, in 4 of 11 sequences. The binding of NADPH creates a bridge between the active-site residues on the right and the α6/α7 subdomain on the left, and this drives the concerted movement of the three regions described above. In doing so, the active-site serine is moved into a location where it could potentially form a hydrogen bond with the carbonyl of the incoming thioester substrate (see text below and Figure 5B), and hydrogen bonds are formed between the 2′ nicotinamide ribose hydroxyl and the OH group of Tyr 151 and the ϵ-NH2 of Lys 155. A final significant interaction is the salt bridge between Arg 15 and the negative charges on both Asp 187 and the pyrophosphate moiety of NADP(H). The salt bridge interaction between Arg 15 and Asp 187 is also present in the cofactor-free conformation, and both residues are strictly conserved in the 11 FabG sequences examined. Arg 15 and Asp 187 are positioned near the amino termini of helices α1 and α6, respectively, and the backbone moves to maintain the electrostatic interaction between these two residues when the cofactor binds (Figure 2).

The cofactor-induced conformational changes have important effects on the orientations of the three active-site residues (Figure 5B). Ser 138, located at the C-terminus of β5, moves by 4 Å, and the hydroxyl group swings around by 180°. Lys 155 does not change its position, but the orientation of the side chain shifts by 90°. Finally, although the α carbon of Tyr 151 does not move, the side chain rotates by 120°. Also clearly visible to the right in the stereoimage presented in Figure 5B is the motion of the β4$-$$\alpha$4 loop. This movement is blocked by the side chain of Tyr 151 in the cofactor-free conformation.

Negative Cooperative Binding of NADP(H) to FabG. The observed conformational changes induced by the binding of cofactor motivated us to investigate the possibility of allostery in the FabG catalytic mechanism. The affinity of *E. coli* FabG for NADPH was determined by fluorescence spectroscopy in the presence and absence of 20 μM ACP (Figure 6). FabG bound NADPH both in the presence and in the absence of ACP, although the shape of the binding curve in the presence of ACP saturated at a lower NADPH concentration. This indicates a negative, heterotropic cooperative effect of ACP on the binding of NADPH (Figure 6A). Analysis of these binding isotherms showed that, in the absence of ACP, the binding of NADPH to FabG exhibited a slight negative, homotropic cooperativity (with a Hill constant of $n_H = 0.9$) (Figure 6B). The low cooperativity observed with NADPH alone could potentially be accounted for by the presence of minor amounts of NADP$^+$ contaminating the NADPH. In contrast, the degree of negative cooperativity was significantly increased by the presence of ACP (the Hill constant, $n_H = 0.7$) (Figure 6C). These data were used to calculate the number of apparent NADPH-binding sites in the presence and absence of ACP (Figure 7). In the absence of ACP, there were 3.8 ± 0.4 NADPH sites (Figure 7A), which corresponds to the number of sites on the FabG tetramer. In the presence of ACP, the affinity for NADPH increased, and the number of these higher affinity sites per FabG tetramer was 1.26 ± 0.16. Taken together, the negative cooperativity and stoichiometry calculations indicate that ACP binding converts the four equivalent NADPH sites on FabG to a single, higher affinity NADPH site in the FabG·ACP·NADPH ternary complex, and that the other three sites on the FabG tetramer exhibit lower affinities for NADPH.

Effect of NADPH on FabG−ACP Interactions. ACP was a mixed inhibitor of the FabG reaction with respect to NADPH, supporting a sequential kinetic mechanism, although ACP does bind to the free enzyme and does not bind to the same site as NADPH. The binding of *E. coli* FabG to ACP was analyzed by surface plasmon resonance both in the presence and in the absence of NADPH (Figure 8). FabG bound to ACP with an apparent K_d of 4.5 μM (Figure 8A)

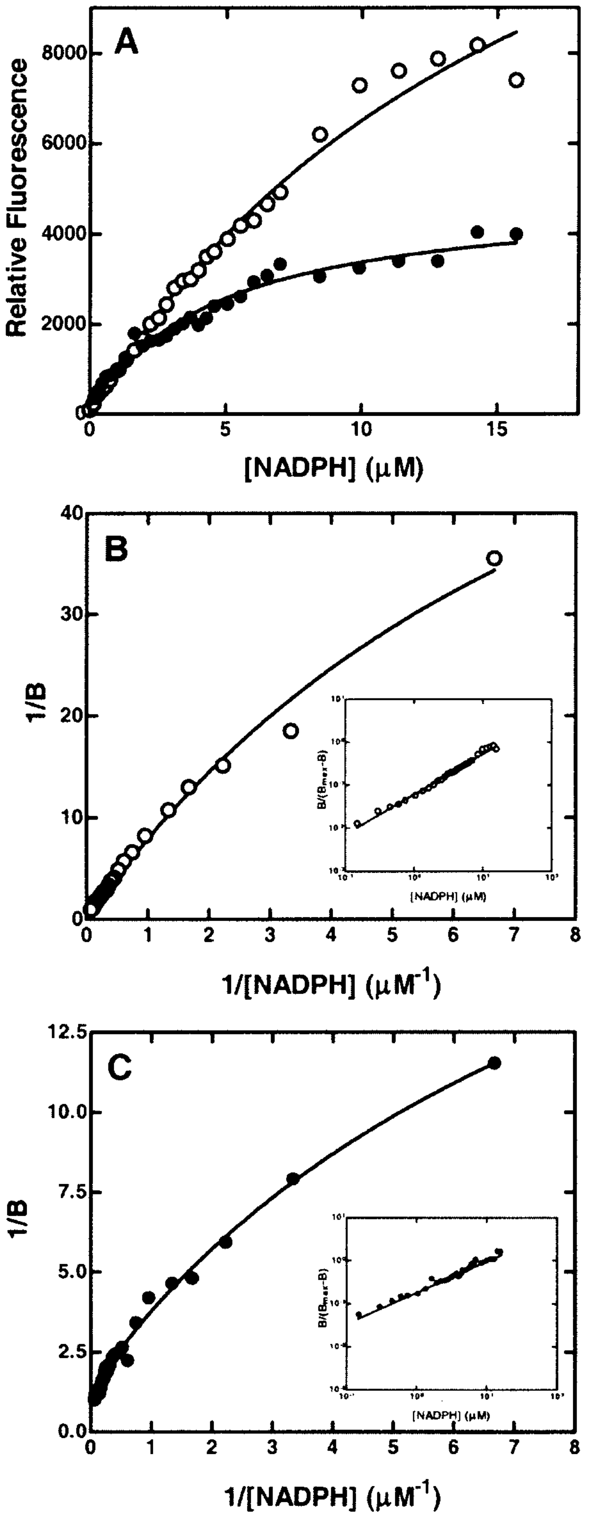

FIGURE 6: Negative cooperative binding of NADPH to FabG. Binding of NADPH to FabG in the absence (○) and presence of 20 μM ACP (●) was studied by fluorescence titration with excitation at 340 nm and emission at 455 nm, as described under Experimental Procedures. The relative fluorescence intensity (observed fluorescence minus the initial fluorescence) was fit using nonlinear regression analysis to the Hill equation (A). The addition of ACP to FabG decreased the maximal binding of NADPH. To make the data easier to compare, the relative fluorescence data were normalized to the total fluorescence change in each experiment and expressed as B (for binding). Double-reciprocal plots of the data showed negative cooperativity of NADPH binding (B and C). Conventional Hill plots of the data are shown as insets with an estimated Hill coefficient of 0.9 and 0.7 in the absence and presence of ACP, respectively.

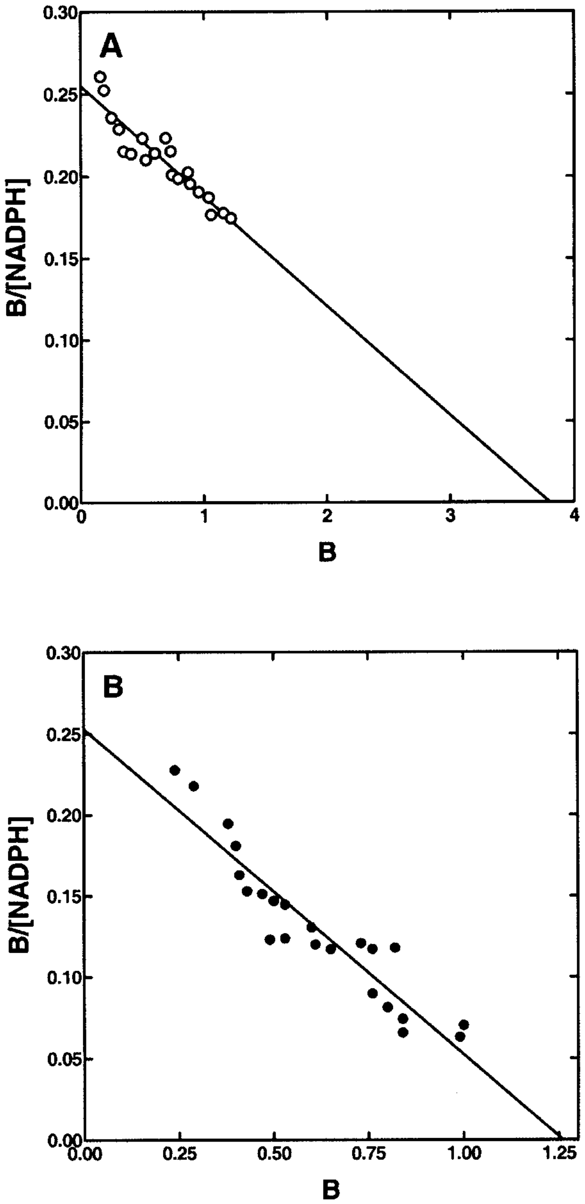

FIGURE 7: Calculation of the binding stoichiometry for NADPH in the presence and absence of ACP. NADPH binding experiments were performed in the absence (panel A) and presence (panel B) of 20 μM ACP and the data analyzed using a Scatchard plot. The number of NADPH binding sites per FabG tetramer was calculated as 3.8 ± 0.4 in the absence of ACP and 1.26 ± 0.16 in the presence of ACP.

in the absence of NADPH. The presence of NADPH (100 μM) had a large effect on the binding of FabG to ACP (Figure 8, panels A and B). The apparent K_d was reduced to 1.6 μM, and the maximum measured binding was reduced by 70%. The inhibitory effect of NADPH on FabG binding to ACP decreased with the NADPH concentration, with an apparent equilibrium constant of 10.2 μM. These data are consistent with a model where the high-affinity binding of ACP to one active site decreases the affinity of the other sites for ACP. This results in ~75% less total ACP binding to FabG and corresponds to a reduction in the number of higher affinity ACP sites from 4 to 1.

This observation was corroborated by performing a similar experiment in solution using AlphaScreen technology. His-tagged FabG and biotinylated-ACP were allowed to bind in

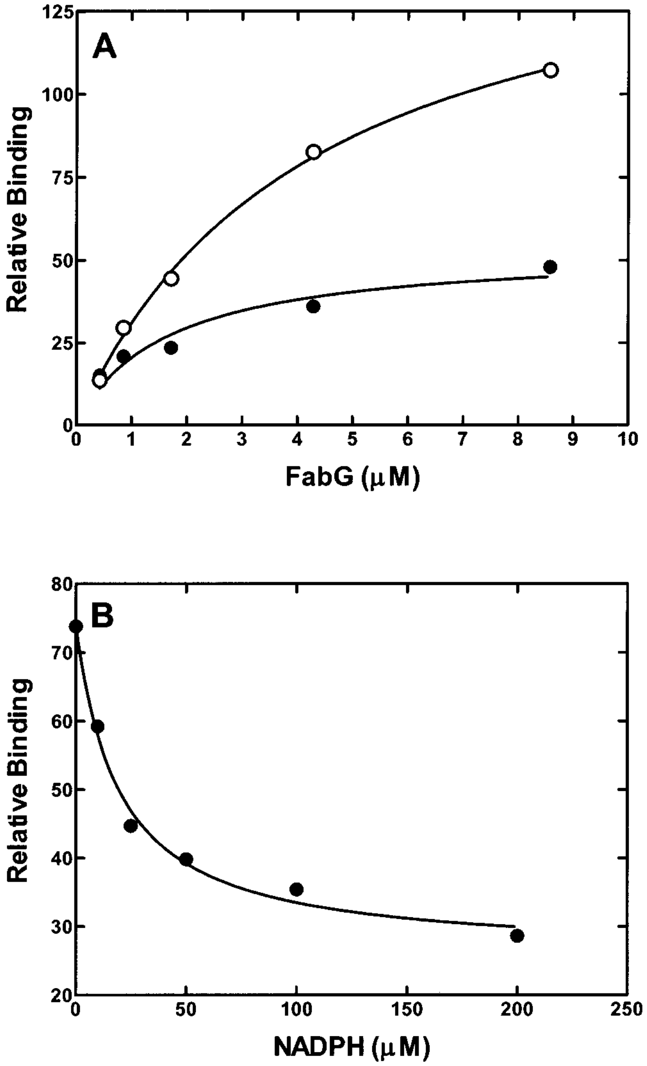

FIGURE 8: Effect of NADPH on FabG binding to ACP. Binding of FabG to ACP at different concentrations of NADPH was measured by real-time biomolecular interaction analysis with the Biacore 3000 instrument as described in the Experimental Procedures. ACP was covalently immobilized to CM-5 chip and solutions of FabG both with (●) and without (○) NADPH were injected. Data reported are differences in the SPR signal between the ACP containing flow cell and the reference cell. (A) FabG showed decreased binding to ACP in the presence of NADPH, and the apparent K_d of FabG to ACP decreased from 4.2 to 1.6 μM. (**B**) The maximal binding signal of FabG to ACP decreased as the NADPH concentration increased. The apparent equilibrium constant for inhibition of FabG binding to ACP by NADPH was 10.2 μM.

the presence of different concentrations of NADPH, and the degree of association was determined by fluorescence resonance energy transfer between donor beads coated with streptavidin and acceptor beads containing bound anti-(His)$_6$-antibody as described in the Experimental Procedures. The addition of NADPH caused a progressive decrease in the total ACP binding to FabG (Figure 9). The apparent equilibrium constant for NADPH inhibition was 3 μM, which was slightly lower than the 10 μM value in Figure 8. The reduction in this experiment was ~75%, which is in close agreement with the surface plasmon resonance experiment (Figure 8). These two technologies point to the number of high-affinity ACP binding sites being reduced from 4 to 1 in the presence of NADPH.

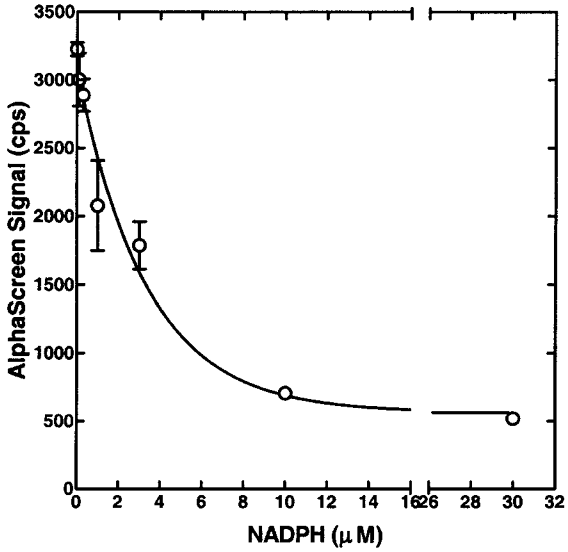

FIGURE 9: Effect of NADPH on ACP binding to FabG using AlphaScreen technology. Biotinylated ACP and His-tagged FabG were mixed and incubated for 30 min as described in the Experimental Procedures. Streptavidin donor beads and anti-(His)$_6$-antibody acceptor beads were then added and the degree of interaction quantitated as a function of NADPH concentration. The apparent equilibrium constant for the inhibition of ACP binding by NADPH was 3 μM.

DISCUSSION

Relation of FabG to the SDR Family. The short-chain dehydrogenase/reductase (SDR) family contains a wide variety of enzymes in organisms ranging from bacteria to mammals (*23*). These molecules share the common function of adding or removing hydrogen in a NAD(H)- or NADP-(H)-dependent manner from specific substrates. Notable medically relevant examples are the steroid dehydrogenases, which are active in controlling high blood pressure and fertility in humans (*24*). Structurally, FabG appears to be a typical example of these proteins, containing approximately 250 amino acids, existing as a tetramer and having an α/β structure with the signature Rossmann fold motif (*7*). This Rossmann fold creates a "topological switch point" at the carboxy termini of two central β strands, and the cleft formed at this point creates a nucleotide-binding site which binds the cofactor (*7*). Also, FabG contains the highly conserved catalytic YX$_3$K motif which is usually present near the carboxy terminus of an α helix (*23*). In FabG, the motif is represented as Tyr 151−X$_3$−Lys 155, and the adjacent helix is α4. Additionally, FabG has a conserved serine residue (Ser 138) positioned near the tyrosine and lysine. This Tyr-Lys-Ser catalytic triad is present in a number of SDR enzymes (*23*). Although the precise catalytic mechanism mediated by these residues is a matter of debate, it appears that the tyrosine and lysine residues are involved in actual catalysis (*25*), whereas the serine participates in substrate binding and alignment (*26*). According to this scheme, Lys 155 and Tyr 151 cooperate to transfer a proton to the keto moiety of the substrate and Ser 138 forms a hydrogen bond with the thioester carbonyl to correctly position the β-ketoacyl-ACP in the active site. Determining the mechanism of the FabG active site will be the focus of our future studies on this enzyme.

Cofactor Binding Drives Conformational Change and Organizes the Active Site. A comparison of our structure of

E. coli FabG lacking cofactor with the recently determined structure of the *B. napus* FabG·NADP$^+$ binary complex reveals that the cofactor binding induces a significant conformational change (Figure 4). There is little doubt that cofactor binding actually drives these conformational changes; as shown in Figure 5A, all of the major interactions between FabG and the cofactor are only possible after the conformational change has occurred in the protein. Also, not apparent in Figures 4 and 5 is the fact that NADPH cannot access its binding site in the structure we determined of *E. coli* FabG (which lacks cofactor) because the loops connecting β4 to α4 and β5 to α5 sterically block the site. Part of the conformational change is the movement of these two loops to allow the binding of cofactor. It is worth noting that the regions of FabG that undergo a conformational change show small but clear differences in the monomers of the ASU (on the order of 1 Å), and some segments are completely disordered. This supports the notion that they are flexible in the absence of cofactor.

An important consequence of the conformational change is the reorientation of the three active-site residues. Tyr 151 and Lys 155 are directly affected since they both interact with the 2′ nicotinamide ribose hydroxyl group of NADP(H) (Figure 5A), whereas the effect on Ser 138 is indirect. By comparing the positions of the three residues before and after the conformational change (Figure 5B), it is apparent that the FabG·NADP$^+$ active site represents the functional state (*9*). In the active-site triad of FabG lacking cofactor, the three side chains are inappropriately oriented to support either cofactor binding or productive catalysis. Most notably, the side chains of Tyr 151 and Lys 155 are pointing in opposite directions (Figure 5B).

Conformational Change May Promote the Binding of Acyl-ACP. The structures of a number of SDR enzymes are known, and none show evidence for the type of cofactor-induced conformational change that we have reported for FabG. For example, the structures of 3α-hydroxysteroid dehydrogenase (*27*), GDP-mannose 4,6-dehydratase (*28*) and 17β-hydroxysteroid dehydrogenase (*29*) all appear to have undistorted cofactor-binding sites in the free form that do not require major reorganization for the formation of the binary enzyme−cofactor complex. The particular reason this mechanism should operate in FabG may be related to the way the lipid substrate is delivered to the active site by a 4′-phosphopantetheine group attached to ACP. Although we have no direct evidence, the structure of the FabG−cofactor complex suggests that the β-keto substrate accesses the active site from above as viewed in Figure 2B. This direction avoids steric clash between the cofactor and the phosphopantetheine group, most easily positions the β-keto group adjacent to the reducing equivalents of the nicotinamide ring, and involves elements of FabG (α6/α7) that are topologically equivalent to the substrate-binding regions of other SDR enzymes. Also, this mode of β-keto-substrate binding is analogous to what is observed in the ternary structure of another SDR enzyme, 7α-hydroxysteroid dehydrogenase (7α-HSDH), with NADH and hydroxysteroid substrate (*30*), which shows the substrate and cofactor accessing the active site from opposite sides. It should be noted that this mode of binding differs fundamentally from the proposal of Fisher and co-workers (*9*) in which both the cofactor and the β-keto substrate approach from the same side (from the front in Figure 2). We believe that their alternate model is untenable for steric reasons.

We have previously shown that ACP recognizes a constellation of surface features on each of its partner enzymes (*31*). Although we have not identified the ACP-binding site on FabG, our proposal for substrate binding would suggest that the α6/α7 subdomain is adjacent to, or forms part of, this site. This, in turn, suggests that the observed conformational change may alter the ACP-binding surface on the enzyme, perhaps to promote its interaction with the β-ketoacyl-ACP substrate. Some members of the fatty acid biosynthetic enzyme group, notably FabA (*32*), FabH (*33*,*34*), FabB (*35*), and FabF (*36*), have their active sites at the base of a hydrophobic tunnel that accommodates the ACP prosthetic group. It is therefore significant that a comparison of the FabG and FabG·NADP$^+$ structures reveals that only the latter has a defined tunnel, and it is created by the movement of the α6/α7 subdomain toward the body of the protein. Thus, the conformational change not only organizes the active-site constellation but it may also be a mechanism that ensures that β-ketoacyl-ACP most efficiently binds to the enzyme in the catalytically productive state. This view is supported by the data shown in Figure 8A, which demonstrates increased binding affinity (lower K_d) of FabG to ACP in the presence of NADPH.

Conformational Change and Cooperativity. The conformational change not only reorganizes the active site and promotes ACP binding but it also appears to provide a structural basis for the transmission of negative cooperativity. FabG is a tetrameric enzyme and the NADPH binding exhibits moderate negative cooperativity (Figure 6). The extensive and intimate subunit−subunit interactions shown in Figure 3 are consistent with the transmission of the conformational change from one monomer to another associated with NADPH binding to an active site. Particularly suggestive is the α6/α7 subdomain that experiences a significant repositioning upon cofactor binding. Tyr 229 spans the monomer-monomer interface and makes a number of specific interactions with the two loops that connect the subdomain to the body of the protein (Figure 3C). It is therefore well positioned to structurally mediate the allostery in FabG.

This negative cooperativity is significantly increased by the presence of ACP (Figure 6), which suggests that an additional conformational change occurs following ACP binding. A similar substrate-induced conformational change has been observed in 7α-HSDH (*30*). A comparison of the binary 7α-HSDH·NAD$^+$ complex with the ternary complex containing both NADH and hydroxysteroid substrate shows that there is a substrate-binding loop which swings toward the active-site cleft upon hydroxysteroid binding. This substrate-binding loop of 7α-HSDH corresponds precisely to the α6/α7 subdomain of FabG in a structural alignment of the two enzymes. The structure of 7α-HSDH in the absence of both cofactor and hydroxysteroid-substrate has not been determined, and it is not known whether a conformational change similar to that observed in FabG occurs in 7α-HSDH upon cofactor binding. However, the existence of substrate induced conformational change in 7α-HSDH strongly suggests that such an effect may also occur in FabG. In addition, our biochemical data presented in Figures 6 through 9 are consistent with a model where the high-affinity binding of ACP to one active site decreases the affinity of the other sites for ACP.

Our structure indicates that the movements associated with NADPH (Figures 3A and 4) and ACP binding could be transmitted within the tetramer to promote the open conformation of the adjacent active site, thus reducing the substrate and cofactor affinities for a site where the reaction is complete. This could provide a mechanism by which product is expelled and the active site cleared to allow the binding of a NADPH molecule and β-keto-substrate for the next catalytic cycle.

ACKNOWLEDGMENT

A.P. would like to thank two instructors at the RAPIDATA2000 course, Hal Lewis at NSLS X25 for his assistance during data collection, and Charles Weeks for his invaluable help running his program, SnB. A.P. would also like to acknowledge both Clemens Vohnrien and Gerard Bricogne for their crucial contributions with the SHARP refinements. We also thank William Lewis for his assistance with the BIACORE experiments. We thank Tuan Tran for his assistance with the AlphaScreen experiments.

REFERENCES

1. Smith, S. (1994) *FASEB J. 8*, 1248−1259.
2. Rock, C. O., and Cronan, J. E., Jr. (1996) *Biochim. Biophys. Acta 1302*, 1−16.
3. Cronan, J. E., Jr., and Rock, C. O. (1996) in *Escherichia coli and Salmonella typhimurium*: cellular and molecular biology (Neidhardt, F. C., Curtis, R., Gross, C. A., Ingraham, J. L., Lin, E. C. C., Low, K. B., Magasanik, B., Reznikoff, W., Riley, M., Schaechter, M., and Umbarger, H. E., Eds.) pp 612−636, American Society for Microbiology, Washington, DC.
4. Alberts, A. W., Majerus, P. W., Talamo, B., and Vagelos, P. R. (1964) *Biochemistry 3*, 1563−1571.
5. Toomey, R. E., and Wakil, S. J. (1966) *Biochim. Biophys. Acta 116*, 189−197.
6. Sheldon, P. S., Kekwick, R. G., Smith, C. G., Sidebottom, C., and Slabas, A. R. (1992) *Biochim. Biophys. Acta 1120*, 151−159.
7. Jörnvall, H., Persson, B., Krook, M., Atrian, S., Gonzalez-Duarte, R., Jeffery, J., and Ghosh, D. (1995) *Biochemistry 34*, 6003−6013.
8. Zhang, Y., and Cronan, J. E., Jr. (1998) *J. Bacteriol. 180*, 3295−3303.
9. Fisher, M., Kroon, J. T., Martindale, W., Stuitje, A. R., Slabas, A. R., and Rafferty, J. B. (2000) *Structure 8*, 339−347.
10. Heath, R. J., and Rock, C. O. (1995) *J. Biol. Chem. 270*, 26538−26542.
11. Leslie, A. G. W., Brick, P., and Wonacott, A. T. (1986) pp 33−39, SERC Daresbury Laboratory, Warrington, U.K.
12. Evans, P. R. (1993) The improved package for the measurement of oscillation photographs. *Proceeding of CCP4 Study Weekend: Data Collection & Processing*, pp 114−122.
13. Weeks, C. M., and Miller, R. (1999) *J. Appl. Crystallogr. 32*, 120−124.
14. Blessing, R. H., Guo, D. Y., and Langs, D. A. (1996) *Acta Crystallogr., Sect. D 52*, 257−266.
15. Otwinowski, Z. (1991) in *Isomorphous Replacement and Anomalous Scattering* (Wolf, W., Evans, P. R., and Leslie, A. G. W., Eds.) pp 80−88, SERC Proceedings, Daresbury Laboratories, Warrington, England.
16. Brünger, A. T., Adams, P. D., Clore, G. M., DeLano, W. L., Gros, P., Grosse-Kunstleve, R. W., Jiang, J. S., Kuszewski, J., Nilges, M., Pannu, N. S., Read, R. J., Rice, L. M., Simonson, T., and Warren, G. L. (1998) *Acta Crystallogr., Sect. D 54*, 905−921.
17. Jones, T. A., Zou, J. Y., Cowan, S. W., and Kjeldgaard, M. (1991) *Acta Crystallogr., Sect. A 47*, 110−119.
18. de la Fortelle, E., and Bricogne, G. (1997) *Methods Enzymol. 276*, 472−494.
19. Laskowski, R. A., McArthur, M. W., Moss, D. S., and Thornton, J. M. (1993) *J. Appl. Crystallogr. 26*, 282−291.
20. Ullman, E. F., Kirakossian, H., Singh, S., Wu, Z. P., Irvin, B. R., Pease, J. S., Switchenko, A. C., Irvine, J. D., Dafforn, A., Skold, C. N., and Wagner, D. B. (1994) *Proc. Natl. Acad. Sci. U.S.A 91*, 5426−5430.
21. Beaudet, L., Bedard, J., Breton, B., Mercuri, R. J., and Budarf, M. L. (2001) *Genome Res. 11*, 600−608.
22. Brünger, A. T. (1988) *J. Mol. Biol. 203*, 803−816.
23. Persson, B., Krook, M., and Jörnvall, H. (1991) *Eur. J. Biochem. 200*, 537−543.
24. Duax, W. L., and Ghosh, D. (1997) *Steroids 62*, 95−100.
25. Chen, Z., Jiang, J. C., Lin, Z.-G., Lee, W. R., Baker, M. E., and Chang, S. H. (1993) *Biochemistry 32*, 3342−3346.
26. Oppermann, U. C. T., Filling, C., Berndt, K. D., Persson, B., Benach, J., Ladenstein, R., and Jörnvall, H. (1997) *Biochemistry 36*, 34−40.
27. Grimm, C., Maser, E., Mobus, E., Klebe, G., Reuter, K., and Ficner, R. (2000) *J. Biol. Chem. 275*, 41333−41339.
28. Somoza, J. R., Menon, S., Schmidt, H., Joseph-McCarthy, D., Dessen, A., Stahl, M. L., Somers, W. S., and Sullivan, F. X. (2000) *Structure 8*, 123−135.
29. Ghosh, D., Pletnev, V. Z., Zhu, D. W., Wawrzak, Z., Duax, W. L., Pangborn, W., Labrie, F., and Lin, S. X. (1995) *Structure 3*, 503−513.
30. Tanaka, N., Nonaka, T., Tanabe, T., Yoshimoto, T., Tsuru, D., and Mitsui, Y. (1996) *Biochemistry 35*, 7715−7730.
31. Zhang, Y.-M., Rao, M. S., Heath, R. J., Price, A. C., Olson, A. J., Rock, C. O., and White, S. W. (2001) *J. Biol. Chem. 276*, 8231−8238.
32. Leesong, M., Henderson, B. S., Gillig, J. R., Schwab, J. M., and Smith, J. L. (1996) *Structure 4*, 253−264.
33. Davies, C., Heath, R. J., White, S. W., and Rock, C. O. (2000) *Structure 8*, 185−195.
34. Qiu, X., Janson, C. A., Konstantinidis, A. K., Nwagwu, S., Silverman, C., Smith, W. W., Khandekar, S., Lonsdale, J., and Abdel-Meguid, S. S. (1999) *J. Biol. Chem. 274*, 36465−36471.
35. Olsen, J. G., Kadziola, A., Wettstein-Knowles, P., Siggaard-Andersen, M., Lindquist, Y., and Larsen, S. (1999) *FEBS Lett. 460*, 46−52.
36. Huang, W., Jia, J., Edwards, P., Dehesh, K., Schneider, G., and Lindqvist, Y. (1998) *EMBO J. 17*, 1183−1191.
37. Esnouf, R. M. (1997) *J. Mol. Graphics Modell. 15*, 132−133.
38. Merritt, E. A., and Bacon, D. J. (1997) *Methods Enzymol. 277*, 505−524.
39. Kraulis, P. J. (1991) *J. Appl. Crystallogr. 24*, 946−950.

BI010737G